Cross-Correlation Between Halo Mass and the Sunyaev-Zel'dovich Effect in the Millennium Gas Simulation

Seth Siegel[1]

ABSTRACT

The Sunyaev-Zel'dovich (SZ) Effect is a particularly promising method of cluster detection and over the past decade considerable advances have been made towards realizing its potential. In this paper we present a new way to use future joint optical and SZ surveys to measure the cross-correlation between observable properties of clusters and their SZ signal through the construction of stacked SZ profiles. We develop a non-parametric technique for inverting these profiles to obtain estimates of the average 3-dimensional pressure distribution of the intracluster gas. We test our method on dark matter halos in a numerical N-body simulation and in doing so obtain a measure of the mass-SZ cross-correlation over the range 1.5×10^{13} $M_\odot$ to 3.5×10^{14} $M_\odot$.

1. Introduction

Clusters of galaxies occupy a unique position as the largest virialized objects in the Universe. This makes them a powerful tool for understanding the hierarchal process of structure formation and the cosmological backdrop in which it occurred. Measurement of the abundance of clusters as a function of mass can place constraints on the amplitude of the initial density perturbations σ_8 and the matter density Ω_M of the Universe (Holder et al. 2001; Voit 2005). Furthermore, understanding how the cluster mass function evolves with redshift provides information on the equation of state of the dark energy (Haiman et al. 2001).

Dark matter forms the primary constituent of clusters and drives the dynamics of their formation. Because dark matter interacts solely through gravity its behavior is relatively easy to predict. However, this weak interaction also prevents direct observation of the majority of a cluster's mass. Luckily clusters possess many other observable properties, each of which provides a proxy for the total mass. Baryons are drawn into the deep potential wells created by the dark matter halos and approximately 15% condense into stars and galaxies that emit visible light. The remaining fraction settles into thermodynamic equilibrium in the intracluster medium. This hot ionized gas emits X-rays through thermal bremsstrahlung radiation and up-scatters cosmic microwave background photons through the Sunyaev-Zel'dovich Effect (SZE).

[1]Department of Physics, University of Michigan, Ann Arbor, MI 48109

To use galaxy clusters to place constraints on cosmology we must understand the scaling relationships between the observables that we measure - such as optical richness, X-ray temperature, and SZ decrement - and the underlying mass of the cluster, along with the scatter in these relationships. Ideally, one would like to obtain a volume-limited catalog of all clusters above some mass threshold M_T. In reality, due to scatter in the observable-mass relationships a fraction of clusters will have mass $M < M_T$ but will be detected because they have been scattered above the threshold. Likewise, a smaller fraction will have mass $M > M_T$ but will be missed because they are scattered below the threshold. The number scattered above is larger than the number scattered below because there are far fewer massive clusters. This effect leads to errors in any estimation of the cluster mass function. While certain methods of cluster detection have smaller scatter than others, none can completely avoid this problem. By using more than one method of cluster detection, however, one can cross-calibrate the mass-observable relationships to obtain improved estimates on cosmological parameters (Majumdar & Mohr 2003; Cunha 2008). While optical surveys have relatively large scatter in their observable-mass relationships, they can effectively detect clusters down to the low mass threshold corresponding to a single galaxy. As a result, they provide an independent cross check on the number density of clusters in the mass range spanned by other methods of cluster detection such as the SZE.

The possibility of identifying a cluster through its spectral distortion of the CMB was first recognized over thirty years ago (Sunyaev & Zeldovich 1972, 1980), but only recently have developments in sub-millimeter and millimeter astronomy made it a feasible method of cluster detection. One of the most attractive features of the SZE is that the resulting spectral distortion is independent of redshift, enabling the detection of distant clusters as easily as nearby ones. Since the SZ flux is proportional to the temperature-weighted mass of the intracluster gas, a very tight relationship is expected to exist between a cluster's total SZ flux and its total mass. Current results from numerical simulations suggest that this relationship is independent of the dynamical state of the cluster and largely insensitive to the complicated heating and cooling processes that occur in cluster cores (Motl et al. 2005; Nagai 2006; Shaw et al. 2008). These properties make the SZE a promising tool for obtaining deep cluster catalogs with a well-defined selection function that is nearly independent of redshift.

Early observations of clusters using the SZE were largely unsuccessful due to noisy detectors, unaccounted systematic errors, contamination from radio point sources, and emissions from extragalactic dust (for excellent reviews of the history of SZ cluster detection see Birkinshaw (1999) and Carlstrom et al. (2002)). Over the past decade considerable advances have been made in controlling these systematic errors and to date there have been a number of high confidence observations of clusters using the SZE (Jones et al. 1993; Grainge et al. 1993; Herbig 1994; Myers et al. 1997; Holzapfel et al. 1997; Komatsu et al. 2001). The next generation of SZ detectors - such as the SZ Array, Apex-SZE, South Pole Telescope, Atacama Cosmology Telescope, and Planck - are currently being developed and employed to map regions of the sky at sub-millimeter and millimeter wavelengths with improved sensitivity and unprecedented precision.

For example, the South Pole Telescope is currently conducting a $1200 - 2000$ deg^2 sub-millimeter survey with the primary purpose of cluster finding. The survey will produce large area CMB maps in 4 frequency bands with a precision of $1'$ and sensitivity of 10 μK (Ruhl et al. 2004). In addition, the entire area covered by the SPT will overlap with the Dark Energy Survey (DES); a large scale optical survey that will use a new 519 megapixel CCD camera mounted on the Blanco 4-m telescope to map out 5000 deg^2 in the g, r, i, z, and y bands. DES will be optimized to obtain photometric redshifts of galaxy clusters out to $z \sim 1.3$ with an expected uncertainty $\sigma_z \sim 0.02$ (The Dark Energy Survey Collaboration 2005).

In future surveys like DES it will prove beneficial to use the information obtained from both optical and SZ cluster detection methods. In order to understand how the cluster mass functions evolves with time, it will be necessary to obtain redshifts for clusters that have been identified through the SZE. This is one area where optical observations will be especially helpful, as recent advances in neural networks and decision tree algorithms have made it possible, given a sufficient spectroscopic training set, to produce photometric redshifts for thousands of clusters with relatively small uncertainty (Niemack et al. 2009).

But optical surveys can do more than just provide follow-up redshifts. The sensitivity of the next generation of sub-millimeter telescopes will enable detection of only the most massive clusters with an expected threshold $M_T \sim 2 \times 10^{14}$ M$_\odot$ (Ruhl et al. 2004; Fowler 2004; Kaneko 2006). Clusters with mass $M < M_T$ will still induce a temperature decrement on the CMB maps, but when compared to the noise present in these maps their signal will fall below the required significance to qualify as a detection. This noise comes from a number of sources, including primary anisotropies in the CMB itself, contamination from radio point sources, and noise from the detector. Of course one can always lower the significance required for a detection. This will no doubt increase the number of clusters found, but it will also increase the number of false detections. Any cluster catalog that is to be used for precision cosmology must be highly complete and highly pure. That is to say the ideal catalog contains every cluster above some mass threshold and contains zero false detections. This sets a lower limit on the significance required for detection and consequently an inherent limit on the mass that the SZE can probe. However, if we already know the locations of clusters from an optical survey then we can measure the *correlation* between these locations and SZ signal, which as we will see, allows us to probe the SZE in the low mass regime.

In this paper we present a novel way to use joint optical and SZ surveys to measure the relationship between optically detected clusters and their gas properties. This method uses the locations and redshifts of clusters obtained through optical surveys to create a stacked profile of the average SZ signal as a function of projected radius from the cluster centers. These profiles can be stacked based on any observable and can be interpreted as the cross-correlation between that observable and the SZE. Any source of noise that is not correlated with the cluster locations will average out of these stacked profiles. So even though low mass clusters do not have a large enough S/N to allow for confident detections individually, the stacked SZ signal around many of them will be substantially larger than that around random locations in the sky.

In addition, since the SZE is independent of redshift the signal associated with an individual cluster will suffer projection effects from all other clusters located along the line of sight. This results in an uncertainty in the magnitude of the SZ flux associated with that cluster and a corresponding uncertainty in the mass that one might assign to it. Due to the isotropy of the universe the stacked SZ profiles will not suffer from these projection effects. Again, the average background signal can be estimated by measuring the signal around many random locations in the sky. A stacked profile's excess signal above this random level is then exactly the average SZ signal associated with the clusters in that stacked sample. What's more is that while individual clusters are not spherically symmetric the stacked profiles of many of them will be so long as the optical cluster detection algorithm does not preferentially find clusters oriented in a particular direction. This assumption of spherical symmetry is powerful in that it allows us to deproject the 2-dimensional SZ profile to obtain the 3-dimensional electron pressure distribution of the intracluster gas. While an individual cluster in the stacked sample may deviate significantly from the electron pressure distribution that is obtained through this inversion process, on average having that observable property will correlate strongly with having that particular pressure distribution. In this way joint optical and SZ surveys can be used to understand mean characteristics of the intracluster gas for a wide range of observables.

The outline for this paper is as follows. In §2 we present an overview of the Sunyaev-Zel'dovich Effect. In §3 we explain how one can measure the observable-SZ correlation through the creation of stacked SZ profiles. In §4 we describe how to invert these profiles to obtain nonparametric estimates of the 3-dimensional electron pressure distribution. In §5 we give a brief description of the Millennium Gas Simulation and in §6 apply our technique to the dark matter halos in the simulation. Finally, we conclude in §7 by generalizing to galaxy clusters in real data and discussing some of the opportunities and challenges inherent in doing so.

2. The CMB and the SZE

2.1. The Cosmic Microwave Background

The cosmic microwave background represents the dominant electromagnetic radiation field in the Universe. Its origin can be traced back to the epoch of recombination, a period of time around $z \simeq 1000$ when the Universe became cool enough for hydrogen and helium nuclei to capture electrons and become neutral.

Before this period baryonic matter (in the form of ionized plasma) and radiation were coupled through Thomson scattering and formed a single "baryon-photon" fluid. The pressure of the radiation field effectively stabilized the gravitational infall of baryons into the dark matter potential wells. When the fluid reached a temperature $T_{rec} \approx 3500$ K it underwent a brief ($z \simeq 100$) phase transition from ionized plasma to neutral gas as the hydrogen and helium nuclei began to capture electrons. During this transition the number density of free electrons dropped to almost zero and

as a result the possibility of interaction between baryons and photons became remote. The photons comprising the radiation field scattered for a final time, forming what is known as the surface of last scattering, while the baryons, free from radiation pressure, proceeded to fall into the dark matter potential wells. The photons free-streamed through the now transparent universe and were redshifted to the microwave region of the spectrum, forming the cosmic microwave background. In a sense the CMB is a picture of the universe as it was at $z \simeq 1000$ or approximately 300,000 years after the Big Bang.

The thermal spectrum of the CMB is a nearly perfect Planck blackbody at temperature $T_{cmb} = 2.725 \pm 0.002$ (Mather et al. 1994; Fixsen et al. 1994). At this temperature the spectrum peaks at a wavelength of 1.9 mm. The CMB is highly isotropic and fluctuations in temperature are small, on the order of tens to thousands of micro-Kelvin. If the CMB radiation were to travel undisturbed from the surface of last scattering to our detectors then these small anisotropies would be a result of processes occurring during the epoch of recombination. However, there are a number of structures in the universe that can affect the propagation of CMB photons, resulting in what are known as secondary anisotropies. On angular scales less than 10° these secondary anisotropies are dominated by the Sunyaev-Zel'dovich effect.

2.2. The Sunyaev-Zel'dovich Effect

Most of a cluster's total baryonic mass resides in the intracluster medium in the form of hot, ionized gas. This gas is the source of thermal bremsstrahlung X-ray emission, the spectra of which suggests temperatures on the order of 10^8 K (Sarazin 1988). The Sunyaev-Zel'dovich effect occurs when CMB photons passing through this gas undergo inverse Compton scattering with free electrons. This boosts the photons to higher energies and shifts the overall blackbody spectrum to higher frequencies. As a result, the observed temperature of the CMB over the solid angle subtended by a cluster is decreased in the Rayleigh-Jean's region and increased for frequencies $\nu \gtrsim 220$ GHz.

If a cluster has electron number density $n_e(\mathbf{r})$ and electron temperature $T_e(\mathbf{r})$ then the Compton y parameter through the cluster is defined as

$$y = \int_{-\infty}^{\infty} n_e(\mathbf{r}) \sigma_T \frac{k_B T_e(\mathbf{r})}{m_e c^2} dl \quad (1)$$

where l is the line of sight, σ_T is the Thomson cross section, k_B is the Boltzmann constant, m_e is the electron mass, and c is the speed of light. The y parameter can be thought of quite simply as the integrated electron pressure along the line of sight. If we ignore kinematic effects that arise from the peculiar motion of the cluster and work in the limit that the scattering electrons behave nonrelativistically then the y parameter is related to the relative temperature decrement (increment) through the relation (Sunyaev & Zeldovich 1980)

$$\frac{\Delta T}{T_{cmb}} \quad = \quad f(x)\ y \tag{2}$$

where $x = h\nu/k_B T_{cmb}$ is a dimensionless frequency and $f(x)$ is the frequency dependence of the spectral distortion, given by the equation

$$f(x) \quad = \quad \frac{x^2 e^x}{(e^x - 1)^2} \left(x \coth \frac{x}{2} - 4 \right). \tag{3}$$

Hence, the ΔT measured at given frequency ν is directly proportional to the y parameter. Figure 1 illustrates how the CMB blackbody spectrum is distorted by the SZE for a highly exaggerated y parameter. The y parameter associated with an actual cluster would typically be three to four orders of magnitude smaller. The temperature decrement ΔT that one might expect to measure in the direction of a cluster of mass $M_T = 1 \times 10^{14}$ $M_\odot$ is also shown in Fig. 1. As you can see it is rather minute, reaching a maximum deviation of only 55 μK in the Rayleigh Jean's region of the spectrum.

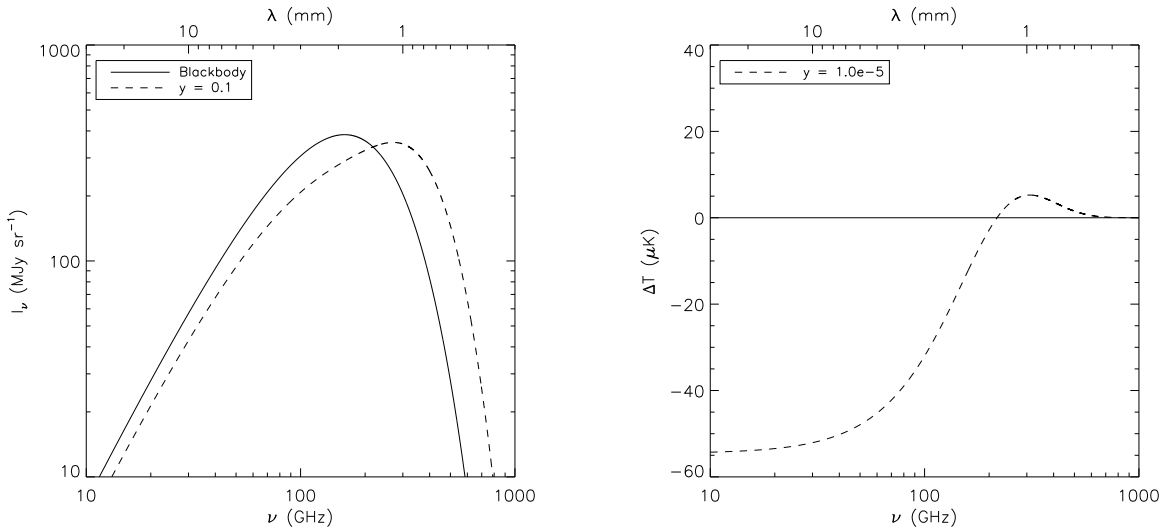

Fig. 1.— The left hand figure shows the Planck blackbody spectrum at a temperature $T_{cmb} = 2.725$ K (solid line) and the distorted blackbody spectrum (dashed line) due to an exaggerated y parameter of 0.1. The right hand figure shows ΔT for a realistic y parameter of 1×10^{-5}, typical for the central value of a cluster of mass 1×10^{14} $M_\odot$.

Since ΔT is proportional to the integrated electron pressure along the line of sight, the SZE can be used to study the pressure distribution of the intracluster gas. To see this more clearly, we write Eq. 1 as

$$y(R) = \frac{\sigma_T}{m_e c^2} \int_{-\infty}^{\infty} k_B \; n_e(R,l) \; T_e(R,l) \; dl \tag{4}$$

$$= \frac{\sigma_T}{m_e c^2} \int_{-\infty}^{\infty} P_e(R,l) \; dl \; . \tag{5}$$

where R is the projected radius from the cluster center. The electron pressure distribution $P_e(R,l)$ of individual clusters will have a wide range of shapes and orientations relative to the line of sight. However, by stacking $y(R)$ from many clusters, the underlying pressure distribution should be spherically symmetric due to the isotropy of the Universe and the linearity of the projection. For the case of stacked profiles we can then assume spherically symmetry, allowing us to make the change of variable $r = \sqrt{R^2 + l^2}$ and obtain

$$y(R) = \frac{\sigma_T}{m_e c^2} \int_{-\infty}^{\infty} P_e(r) \; dl$$

$$= \frac{2 \; \sigma_T}{m_e c^2} \int_{R}^{\infty} \frac{P_e(r) \; r \; dr}{\sqrt{r^2 - R^2}} \tag{6}$$

In this form it becomes evident that $y(R)$ is the Abel projection of $\sigma_T P_e(r)/m_e c^2$ onto the plane perpendicular to the line of sight. As a result, the average 3-dimensional electron pressure $P_e(r)$ of the stacked clusters can be obtained using the Abel inversion

$$P_e(r) = -\frac{m_e c^2}{\pi \sigma_T} \int_{r}^{\infty} \frac{y\,'(R) \; dR}{\sqrt{R^2 - r^2}} \; . \tag{7}$$

Therefore, we can measure the average electron pressure distribution associated with some observable by constructing a stacked profile $y(R)$ for all clusters with that observable and then performing the integral transform given by Eq. 7.

3. Observable - SZ Correlation

Given a catalog of cluster locations and redshifts we measure the correlation between an observable property X of a cluster and its Compton y-parameter through the construction of stacked SZ profiles. The optically identified cluster catalog is first binned logarithmically in X. The mean y parameter as a function of projected radius R is then measured for all clusters that fall in the range $[X - \frac{dX}{2}, \; X + \frac{dX}{2}]$. In this process we use the location of the brightest central galaxy (BCG) as the cluster center and let the projected radius $R = \theta / d_A(z)$ where $d_A(z)$ is the angular diameter distance to the cluster.

Since the Compton y-maps are pixelized, care must be taken in how the stacked profiles are created. The value of each pixel is the average y parameter within that pixel, i.e.

$$y_{pix} = \frac{\int y \, d\Omega}{\Omega_{pix}} \tag{8}$$

where Ω_{pix} is the solid angle that the pixel subtends in the sky. If the width of the radial bins are much larger than the size of the pixels, then we can simply associate the value of a given pixel with its central RA/DEC position. However, in order to obtain as many data points as possible in the region near the cluster, it will be necessary to use bin sizes that are on the order of the pixel width. In this case it would be inaccurate to place the entire SZ flux associated with a pixel into whatever radial bin its central value might fall into.

Instead, for a given cluster (call it cluster i) and a given radial bin ranging from $R_{min} = R - \frac{dR}{2}$ to $R_{max} = R + \frac{dR}{2}$ we construct an annular ring by specifying an n_1 point polygon circumscribed within the circle of radius $\theta_{min} = R_{min}/d_A(z_i)$ from the cluster center and an n_2 point polygon circumscribed within the circle of radius $\theta_{max} = R_{max}/d_A(z_i)$ from the cluster center. We then use a Sutherland-Hodgman polygon clipping algorithm to determine the fractional area F_{pix} of all pixels that overlap with this ring. The final value of this radial bin for the ith cluster is then

$$y_i = \frac{\sum y_{pix} \, F_{pix} \, \Omega_{pix}}{\sum F_{pix} \, \Omega_{pix}} \tag{9}$$

where the sums run over all pixels that overlap with the annular ring. The value of the radial bin for the stacked SZ profile is found by taking the arithmetic average of y for the N clusters falling in the observable bin, i.e.

$$\bar{y} = \frac{1}{N} \sum_{i=1}^{N} y_i \ . \tag{10}$$

The error assigned to this value is just the standard error of the mean, given by

$$\sigma_{\bar{y}} = \frac{1}{N} \sqrt{\sum_{i=1}^{N} (y_i - \bar{y})^2} \tag{11}$$

This process is repeated for all radial bins. It is then repeated for all observable bins. This creates a correlation between the observable X and $y(R)$. Theoretically this process can be used to obtain the correlation between SZ signal and any observable, such as luminosity, richness, X-ray temperature, X-ray luminosity, etc.

4. 3D Inversion

There are a number of ways one can go about evaluating Eq. 7 to obtain the electron pressure distribution from the measured y-profiles. One option is to fit $y(R)$ to a model whose Abel transform has a known, analytic solution. Historically, the isothermal beta model (Cavaliere & Fusco-Femiano 1976, 1981) has been the standard choice for fitting profiles of the intracluster gas, whether they have been obtained from X-ray emission or the SZE. This model assumes that the electron temperature is a constant T_e and that the electron number density follows the spherically symmetric distribution given by

$$n_e(\mathbf{r}) \quad = \quad n_{e0} \left(1 + \frac{r^2}{r_c^2}\right)^{-\frac{3}{2}\beta} \tag{12}$$

where r_c is the cluster core radius and n_{e0} is the central electron number density. This model has an analytic solution to Abel's transform and results in the circularly symmetric observations

$$y(R) \quad = \quad y_0 \left(1 + \frac{R^2}{r_c^2}\right)^{\frac{1}{2}-\frac{3}{2}\beta} \tag{13}$$

where y_0 is the central value of the y parameter, given by

$$y_0 \quad = \quad k_B \, T_e \, n_{e0} \, r_c \, \sqrt{\pi} \, \frac{\sigma_T}{m_e c^2} \, \frac{\Gamma(3\beta - \frac{1}{2})}{\Gamma(3\beta)}. \tag{14}$$

Fitting the measured correlation function to Eq. 13 and taking the best-fit values for y_0, r_c, and β then yields the electron pressure distribution through Eq. 12 and 14. This method is relatively straightforward and we found that the isothermal beta model provided an excellent fit in all cases. Still there are a number of drawbacks to this parametric approach. A large degeneracy exists between the cluster core radius r_c and β so that a wide range of values correspond to a 'good' fit. In addition, the assumption of isothermality only holds out to the virial radius of the cluster. Therefore at large radii the model fails to be an accurate representation of the underlying distribution. Finally, by fitting a model we artificially smooth the data and as a result any subtle features that may be present in the profile is lost.

An alternate approach is to use a non-parametric characterization of the data. This avoids having to impose a priori a specific model onto the intracluster gas or make simplifying assumptions about its behavior. We examine two different non-parametric estimators; the piecewise power-law (PPL) and the cubic spline (CS). Each of these has its own advantages and disadvantages and in many ways the two are complementary to one another.

Suppose we have measured a set of N data points $y_i = y(R_i)$ from a stacked profile. Obtaining the pressure distribution at the points $r_i = R_i$ requires evaluating the equation

$$\begin{aligned} P_e(r_i) &= -\frac{m_e c^2}{\pi \sigma_T} \int_{R_i}^{R_N} \frac{y'(R)}{\sqrt{R^2 - r_i^2}}\, dR \; - \; \frac{m_e c^2}{\pi \sigma_T} \int_{R_N}^{\infty} \frac{y'(R)}{\sqrt{R^2 - r_i^2}}\, dR \\ &\equiv T_D + T_C \end{aligned} \tag{15}$$

where T_D is obtained from the data and T_C is an end correction that accounts for the fact that we only measure $y(R)$ out to a finite radius.

Now given any two points y_i and y_{i+1} we can specify a unique power-law $y(R) = A_i R^{\gamma_i}$ where

$$\gamma_i = \frac{\ln(\, y_{i+1}/y_i \,)}{\ln(\, R_{i+1}/R_i \,)} \qquad\qquad A_i = y_i R_i^{-\gamma_i}$$

The PPL describes $y(R)$ between any two consecutive data points with their unique power-law. The equation for T_D becomes

$$T_D = -\frac{m_e c^2}{\pi \sigma_T} \sum_{j=i}^{N} \left[A_j \gamma_j \int_{R_j}^{R_{j+1}} \frac{R^{\gamma_j - 1}}{\sqrt{R^2 - r_i^2}}\, dR \right] . \tag{16}$$

Unfortunately, the integrals in Eq. 16 do not have analytic solutions and must be evaluated numerically. Note that the singularity that occurs when $j = i$ can be avoided by a simple change of variable. Propagation of error must also be handled numerically and is accomplished using a symmetric differencing scheme.

This method is motivated by the fact that the correlation functions appear to have power-law behavior for a large range of radii. Over this range the PPL will provide a very accurate representation of the the data. In addition, this method minimizes correlating errors between neighboring points. On the other hand, in the core of the cluster and at very large radii the correlation function tends to deviate from power-law behavior. In these regions the PPL will yield a jagged approximation that is not representative of the true shape.

One advantage of using the cubic spline is that it *forces* a smooth curve by requiring continuity between intervals. Given any two points y_i and y_{i+1} we describe the profile between them with the equation

$$y(R) = a_i R^3 + b_i R^2 + c_i R + d_i \tag{17}$$

where the the coefficients in this polynomial are obtained by constraining the first and second derivatives at R_i and R_{i+1} to equal those in the neighboring intervals (see Numerical Recipes (2007)). The resulting expression for T_D is

$$T_D = -\frac{m_e c^2}{\pi \sigma_T} \sum_{j=i}^{N} \left[\int_{R_j}^{R_{j+1}} \frac{3\ a_j\ R^2 + 2\ b_j\ R + c_j}{\sqrt{R^2 - r_i^2}}\ dR \right] . \quad (18)$$

These integrals have analytic expressions, which make evaluating them and propagating errors straightforward.

Calculating the end correction T_C requires extrapolating beyond the measured data. For the case of the stacked SZ profiles this will not be a serious problem because $y(R)$ approach a constant background level at large radii. When this happens $y'(R) = 0$ and their is no contribution to the integral. This convergence occurs rather quickly, but even if a non-negligible signal exists beyond R_N it should only effect the outermost data points due to the fact that the denominator of the integrand in the expression for T_C become large for small r_i.

We estimate T_C in our inversion algorithm by fitting the last N_{end} data points to a power law using a Levenberg-Marquardt least squares technique. We extrapolate $y(R)$ with this best-fit power law from R_N to ∞. The value of T_C is then given by an analytic expression minus a small correction that can be computed numerically.

The isothermal beta model is an excellent tool for testing the accuracy with which these non-parametric inversion methods reproduce the underlying pressure distribution. By creating a 'mock' y-profile from Eq. 13, we can invert it using the PPL/CS method and compare the resulting pressure distribution to the true pressure distribution. It can be shown from Eq. 12 and 14 that this true distribution is given by

$$P_e(r) = \frac{\Gamma(3\beta)}{\sqrt{\pi}\ \Gamma(3\beta - \frac{1}{2})} \frac{m_e\ c^2\ y_0}{\sigma_T\ r_c} \left(1 + \frac{r^2}{r_c^2}\right)^{-\frac{3}{2}\beta} . \quad (19)$$

Our mock y-profile is created using the parameters $y_0 = 5 \times 10^{-5}$, $r_c = 250$ kpc, and $\beta = 2/3$. The continuous function given by Eq. 13 is converted into discrete data points by taking its average value within 100 radial bins of width 50 kpc spanning the range 0 Mpc $\leq R \leq$ 5.0 Mpc. This average bin value is the same quantity that the stacking procedure outlined in §3 should be measuring. The true pressure distribution with which we will compare the inverted profiles is created by applying this discretization procedure to Eq. 19.

The actual profiles that we plan to measure will have errors associated with them that scale as one over the square root of the number of clusters stacked. The integral transform used to invert the

profile will no doubt amplify these errors. In order to explore the magnitude of this amplification we include errors in our mock profile by offsetting each value of y by a random Gaussian with standard deviation $\sigma(R) = f \times y(R)$. We let the percent error f take on several values in the range 0.001 to 0.05. This is consistent with the range of percent errors measured in §6 for the stacked profiles from our N-body simulation.

We display the results of this test in Fig. 2. The top panels show the inverted profiles that result when we ignore the end correction. Over the range $r_c \leq R \leq 1$ Mpc both inversion methods yield a fairly accurate representation of the true distribution, deviating by less than 5%. For $R < r_c$ the PPL method overestimates the true distribution by up to 15% because the isothermal beta model does not have power-law behavior in the cluster core. For $R > 1$ Mpc the errors diverge for both inversion methods, reaching an 80% underestimation at $R = 5$ Mpc. This suggests that, at least for the isothermal beta model, end corrections are necessary.

The middle panels confirms that when end corrections are taken into account the inverted profiles are indistinguishable from the true pressure distribution. This is largely due to the fact that for $R >> r_c$ the isothermal beta model has power-law behavior and as a result the extrapolation is an excellent approximation to the true value. Nevertheless this shows that in principle both the PPL and CS inversion methods work and are capable of obtaining the correct electron pressure to a high degree of accuracy.

The bottom panels display the results when random Gaussian errors with $\sigma(R) = 0.01 \times y(R)$ are introduced prior to the inversion process. The amplification of these errors by the integral transform is clearly evident from the right hand plot. For the most part the amplified errors are less than 10% and there does not appear to be any trend to overestimate or underestimate. The inverted profiles deviate from the true distribution less for the inner radii and more for the outer radii, with the exception of $r < r_c$ for which the errors increase with both methods. An interesting result is that the PPL amplifies errors slightly more than the CS at all radii. We obtain similar results for other values of f and find that on average the error amplification increases almost linearly with radius from a factor of ~ 3 to a factor of ~ 11 for the CS method and from a factor of ~ 4 to a factor of ~ 13 for the PPL method.

These tests suggest that the CS method is a better choice for performing the Abel inversion. It results in less error amplification and models the data accurately over a wider range. In addition, it allows both the integral transform and the propagation of errors to be handled analytically. The main reason for using the PPL is that we expect the profiles to have power law behavior over a wide range of radii. But examining the middle panels of Fig. 2 it is clear that the CS can model this behavior just as well as the PPL. Based on these considerations we will use the CS inversion method throughout the remainder of this paper.

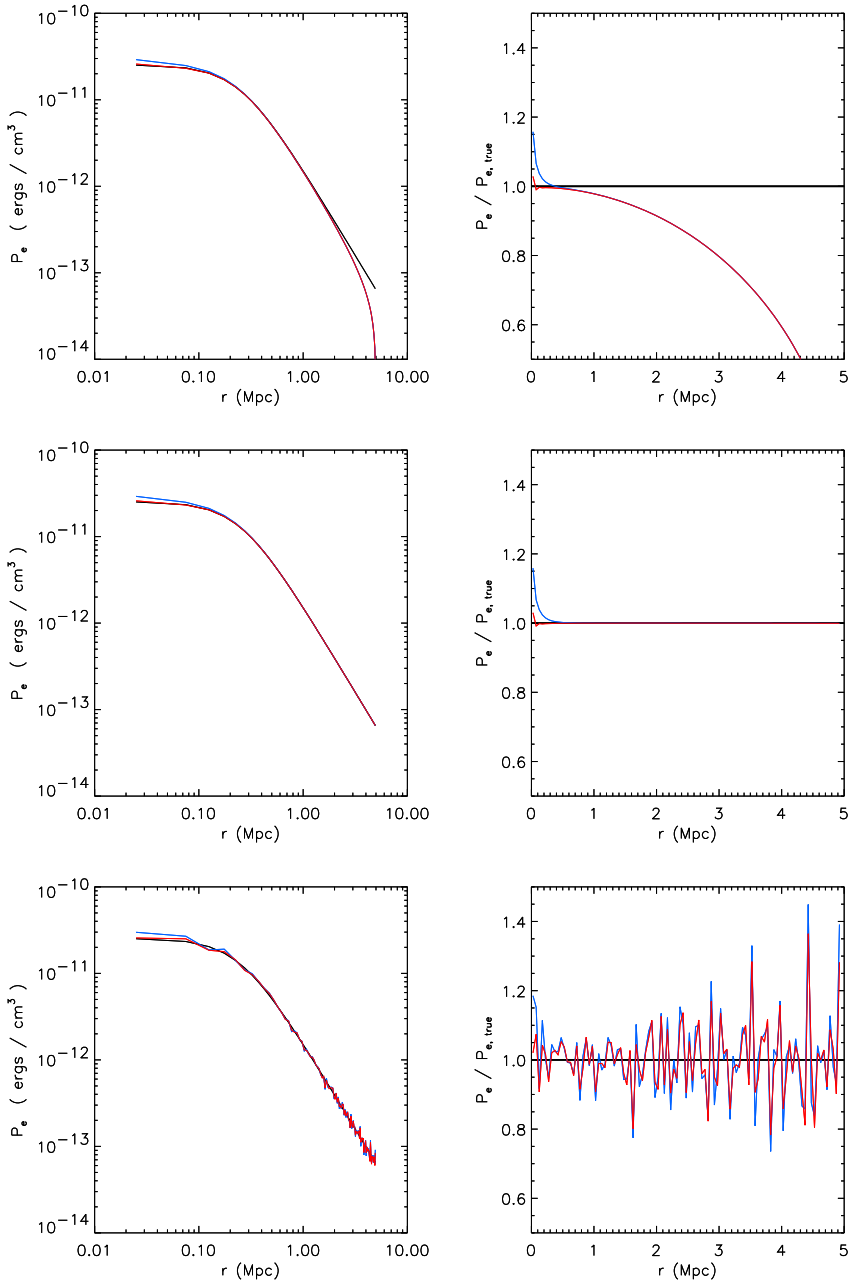

Fig. 2.— We show the electron pressure distribution of an isothermal beta model obtained using the PPL inversion method (light blue), the CS inversion method (red), and the true analytic expression (black). *Top panels*: The inverted profiles are estimated without end corrections (i.e. $P_e = T_D$). *Middle panels*: The inverted profile are estimated with end corrections (i.e. $P_e = T_D + T_C$). *Bottom panels*: Random Gaussian errors with $\sigma(R) = 0.01 \times y(R)$ are introduced prior to inversion. Inverted profiles are estimated with end corrections.

5. The Millennium Gas Simulation

The Millennium Gas Simulation (MGS) is a resimulation of the original, dark matter-only Millennium Simulation (Springel et al. 2005). It follows the evolution of 5×10^8 dark matter particles of mass $1.422 \times 10^8\ h^{-1}\mathrm{M}_\odot$ and 5×10^8 gas particles of mass $3.12 \times 10^9\ h^{-1}\mathrm{M}_\odot$ from $z = 49$ to $z = 0$. The simulation occurs in a $(500\ h^{-1}\ \mathrm{Mpc})^3$ box and assumes a cosmology characterized by the parameters $\Omega_M = 0.25$, $\Omega_\Lambda = 0.75$, $\Omega_b = 0.045$, $h = 0.73$, $\sigma_8 = 0.9$, and $n = 1$ (Stanek et al. 2009).

Data from the simulation is output at 60 redshifts between $z = 2.3$ and $z = 0$. At each output dark matter halos are identified as spherical regions centered on peaks in the dark matter distribution in which the mean density is 500 times the critical density. Graduate student Brian Nord uses the 60 data outputs to model the SZE and calculate the integrated electron pressure along the line of sight. The end result is a catalog of dark matter halos along with a Compton y-map of the sky.

The y-map can be transformed into a map of the temperature decrement ΔT using Eq. 2. To more realistically model the maps that will be obtained from future, large-scale sky surveys one can smooth the map with a Gaussian beam and add instrument noise, CMB noise, and point source contamination. For this paper our main goal is to demonstrate inversion of the stacked profiles and estimate the errors introduced by the this process. As a result, we work with the noise-free Compton y-map.

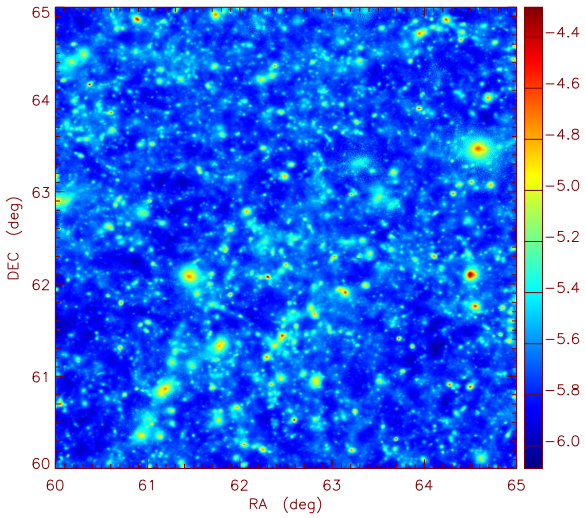

Fig. 3.— Compton y-map for a 25 deg^2 patch of sky from the Millennium Gas Simulation. Scale is in $\log_{10}$ units ranging from $10^{-6.1}$ to $10^{-4.3}$.

6. Results

We apply the techniques outlined in §4 and §5 to 4490 dark matter halos between $0.3 < z < 2.3$ in a $(5 \text{ deg})^2$ patch of sky from the Millennium Gas Simulation. The Compton y-map contains 810,000 pixels and achieves a resolution of $20''$ (see Fig. 3). We use the total mass of the halo as the 'observable' on which we bin. In reality we would not be able to detect the dark matter halos directly, nor measure their total mass. For this exercise we merely wish to demonstrate the stacking and inversion process for the theoretically cleanest scenario. We will generalize to clusters in simulation and real data in the following section. The halos range in mass from 1.5×10^{13} $M_\odot$ to 3.5×10^{14} $M_\odot$ and are placed into 6 logarithmically spaced bins. The stacked profiles are measured in 100 radial annuli of width 50 kpc spanning the range 0 Mpc $\leq R \leq$ 5.0 Mpc

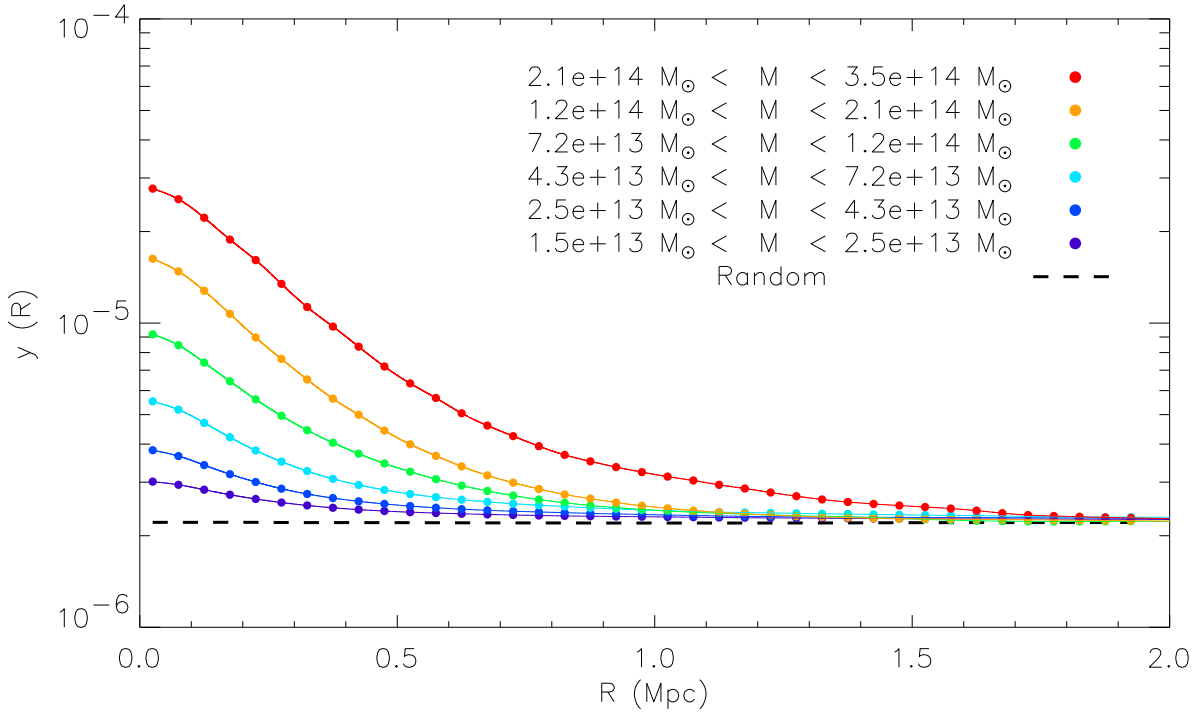

Fig. 4.— We show the stacked profiles of $y(R)$ for 6 halo mass bins ranging from 1.5×10^{13} $M_\odot$ to 3.5×10^{14} $M_\odot$. The filled circles denote measured data points while the solid lines represent the cubic spline interpolations. For comparison, the stacked profile from 10,000 random locations in sky is displayed as a black dashed line.

Figure 4 illustrates the halo mass-SZ correlation. The black dashed line is the stacked profile from 10,000 random locations in the sky. It denotes the average background level and signifies a null correlation. For $R < 1$ Mpc the values of $y(R)$ are significantly larger then this null level for *all* mass bins. Moreover at any given radius there is a very clear scaling between mass and the value

of y. Indeed the y-profiles all appear self-similar, that is they have the same characteristic shape only scaled up for more massive halos. The possible exception to this is the top mass bin (denoted in red), where there appears to be larger values of y at outer radii then would be expected. This is due to poor statistics; there are only 15 halos in this bin. Within this sample there are two cases where a pair of massive halos fall within several megaParsecs of each other. As a result the correlation is increased substantially at outer radii and the sample size is insufficient to average it out.

Perhaps the most interesting aspect of this plot is that even the bottom bin, which contains halos with an average mass of 2×10^{13} $M_\odot$, has a positive correlation and a well-defined profile. Any attempt at detecting these halos from the Compton y-maps alone would most certainly fail because the signal is far too small, having an average peak of less than twice the background level. But since there are so many of them (2290 in fact) we are able to measure a clear signal so long as we already know where to look in the sky. In this exercise we had a list of locations for all halos in the simulation, but in reality we would use an optical cluster catalog which would have a lower mass threshold than the SZE. This demonstrates that the stacked profiles are an excellent way to probe the SZE in the low mass regime. More importantly by inverting these profiles we can learn about the electron pressure of the intracluster gas for the smallest halos all the way to the most massive.

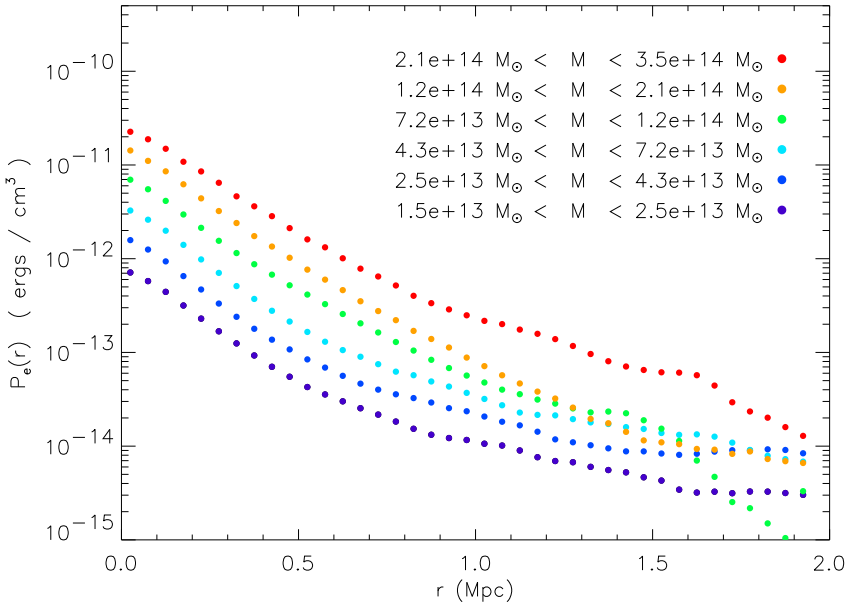

Fig. 5.— We show a log-normal plot of the electron pressure distribution obtained by inverting the stacked profiles of the 6 halo mass bins ranging from 1.5×10^{13} $M_\odot$ to 3.5×10^{14} $M_\odot$.

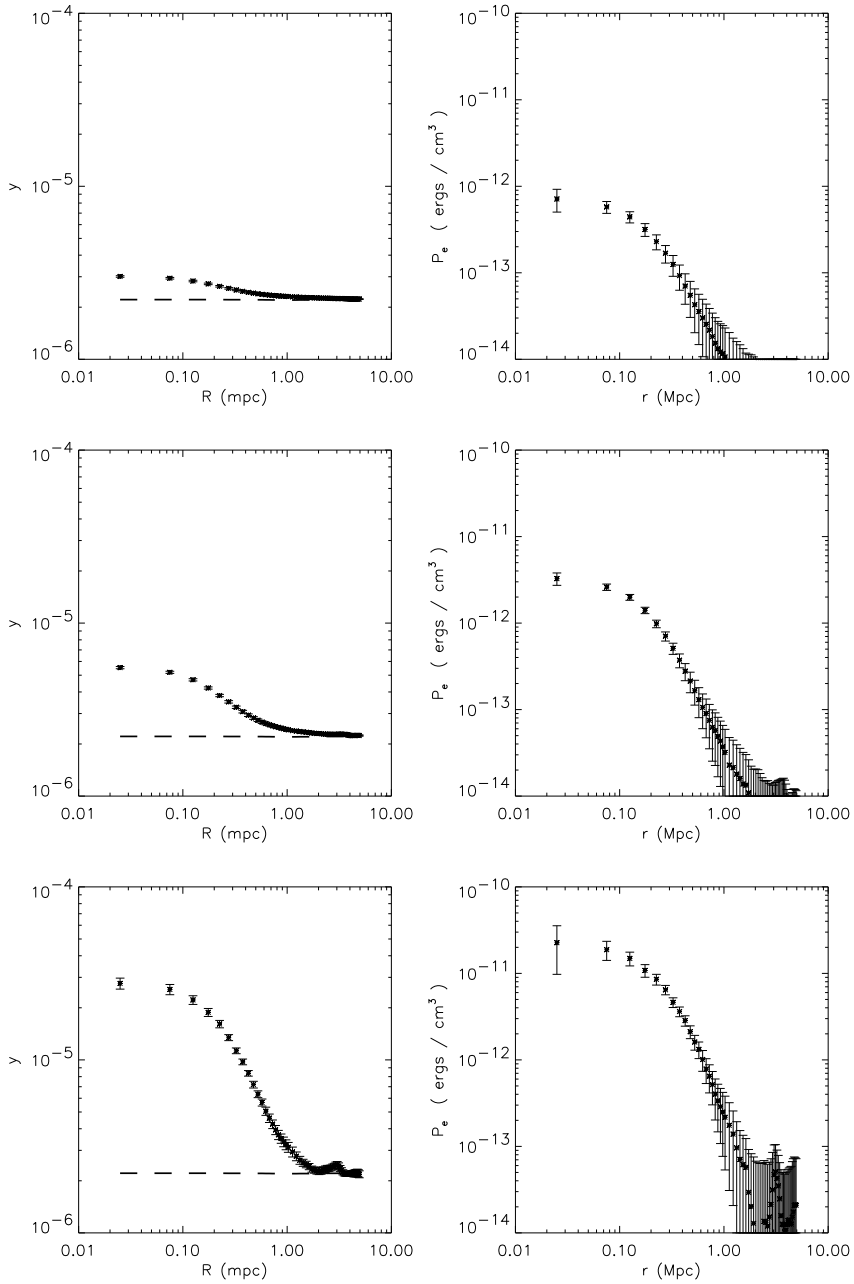

Fig. 6.— We show log-log plots of y-profiles (left) and inverted pressure distributions (right) of three mass bins. *Top panels*: Bin containing 2290 halos with an average mass of $2 \times 10^{13} M_{\odot}$. *Middle panels*: Bin containing 540 halos with an average mass of 5.44×10^{13} $M_{\odot}$. *Bottom panels:* Bin containing 15 halos with an average mass of 2.44×10^{14} $M_{\odot}$.

The CS inversion algorithm is applied to the stacked y-profiles to obtain the average 3-dimensional electron pressure distribution of the halos, pictured in Fig. 5. We used the power-law fit end correction summarized in §4 with $N_{end} = 10$. We found that for $r < 1$ Mpc the pressure was largely insensitive to this end correction. Beyond ~ 1 Mpc it is difficult to make any statement about the behavior of the pressure distribution because the data becomes dominated by errors. This is easiest to see in Fig. 6 which displays both the 2-dimensional profile and the 3-dimensional pressure with errors for three of the mass bins. The pressure distribution of the halos also appear to be self-similar, with a core region that ranges from 200 kpc to 400 kpc followed by a region of power-law behavior as we initially expected.

7. Conclusions

We have outlined a method for measuring the observable-SZ cross-correlation through the construction of stacked profiles of $y(R)$. We have also developed a non-parametric technique for applying Abel's inversion to these profiles to recover the average electron pressure distribution of the intracluster gas. Using a numerical N-body simulation with gas physics we have demonstrated proof of concept by measuring the cross-correlation between halo mass and SZ signal. It was shown that even the smallest halos have a positive correlation with SZ signal and a well defined y-profile.

The next logical step is to apply this technique to the entire Millennium Gas Simulation as opposed to only 25 deg^2. The increased statistics will enable a more accurate determination of both the cross-correlation and the average electron pressure distribution. This will be especially informative for the very massive halos, since we were unable to obtain a significant sample of them within our limited area. We also plan to compare the inverted profiles to the true 3-dimensional electron pressure of the gas. This can be measured directly by going into the simulation and averaging the pressure in 3-dimensional spherical shells about the halo centers. Showing that these two are equal provides an important check on our method and establishes that from the 2-dimensional Compton y-map and cluster locations alone it is possible to reproduce the average 3-dimensional pressure.

Successfully generalizing this technique to galaxy clusters in real data has several important implications, especially if it is used in conjunction with other cross-correlation measurements. Obtaining $P_e(r) = k_b\ n_e(r)\ T_e(r)$ for a large sample of galaxy clusters through the method outlined above and measuring the temperature $T_e(r)$ of the intracluster gas for this same sample would yield the electron number density $n_e(r)$. This is an important quantity because it can be related to the cluster gas mass through the relation

$$M_{gas}(r) \quad = \quad \alpha\ m_p\ n_e(r) \tag{20}$$

where $\alpha \approx 1.3$. One possible way to obtain $T_e(r)$ is through the construction of stacked X-ray

profiles. Rykoff et. al (2008) used the ROSAT All-Sky Survey to stack X-ray emission from clusters in an optically selected catalog and derive scaling relationships between observables such as optical richness and X-ray luminosity. They found that it was difficult to measure cluster temperatures accurately using ROSAT data due to its lack of sensitivity to hard X-rays and the complicating nature of the stacking procedure. Nevertheless, using future X-ray telescopes one might very well be able to make these average temperature measurements. For example, the eROSITA X-ray telescope is scheduled to launch in 2011 as part of the Russian Spectrum-RG mission (Pavlinsky et al. 2006). Over a three year period it will perform a $20,000$ deg^2 survey of the extragalactic sky and is expected to detect tens of thousands of clusters out to $z > 1$. It will have an angular resolution of $15''$ and a sensitivity that is 30 times greater than the ROSAT All-Sky Survey, making it a excellent instrument for obtaining cross-correlation measurements of the temperature of the intracluster gas.

Combining a measurement of the cluster gas mass with a weak lensing measurements of the total mass would then yield the gas mass fraction $f_{gas} = M_{gas}/M_T$. Johnston et. al (2007) outlines a technique similar to the one presented in this paper for measuring the total cluster mass by inverting weak-lensing cross-correlation measurements. They then apply this technique to an optically selected catalog to obtain the mean scaling relationships between optical richness and mass. One can imagine taking an optically identified cluster catalog and combining information on the dark matter halos obtained from weak-lensing cross-correlation measurements with information on the intracluster gas obtained from SZ cross-correlation measurements to learn a great deal about the mean properties of clusters over a large range of an observable such as richness.

Complications will no doubt arise when applying this technique to actual galaxy clusters. One of the main challenges will be dealing with miscentering issues. For some clusters it will be the case that the center of the gas distribution does not coincide with the location of the brightest central galaxy. If we stack these miscentered clusters with clusters that have been centered correctly the net result will be to smear out the cluster core in the y-profile. It will be necessary to estimate the magnitude of this effect in order to correctly interpret the inverted pressure distribution. We plan to explore issues such as miscentering in the near future by adding galaxy clusters to the Millennium Gas Simulation.

Within the next five years the South Pole Telescope, Dark Energy Survey, and eROSITA satellite will map out a large portion of the sky over a wide range of the electromagnetic spectrum from microwaves to X-rays. The number of galaxy clusters detected through each of these surveys individually will be enormous and combining the three will enable calibration of the observable-mass relationships and improved constraints on cosmological parameters. Due to the sheer number of statistics, cross-correlation measurements are a natural and effective way to combine the resulting data sets. They avoid many of the problems thats plague individual observations, such as projection effects, lack of signal, and uncertainty in orientation, and will allow for very accurate determination of an array of cluster properties.

8. Acknowledgments

I would like to give my deepest thanks to Professor Tim McKay for his guidance and support over the past two years. He has taught me a tremendous amount about physics and cosmology and has had a profound influence on my life. I would also like to acknowledge the work of Brian Nord. His modeling of the Sunyaev-Zel'dovich effect was critical to my research and I greatly appreciate his help. Finally, I would like to thank Professor Gus Evrard, Professor David Gerdes, Jiangang Hao, and Dave Johnston for their expertise and advice.

REFERENCES

Birkinshaw, M. 1999, Phys. Rep., 310, 97

Carlstrom, J. E., Holder, G. P., & Reese, E. D. 2002, ARA&A, 40, 643

Cavaliere, A. & Fusco-Femiano, R. 1976, A&A, 49, 137

—. 1981, A&A, 100, 194

Cunha, C. 2008, ArXiv e-prints

Fixsen, D. J., Cheng, E. S., Cottingham, D. A., Eplee, Jr., R. E., Isaacman, R. B., Mather, J. C., Meyer, S. S., Noerdlinger, P. D., Shafer, R. A., Weiss, R., Wright, E. L., Bennett, C. L., Boggess, N. W., Kelsall, T., Moseley, S. H., Silverberg, R. F., Smoot, G. F., & Wilkinson, D. T. 1994, ApJ, 420, 445

Fowler, J. W. 2004, in Society of Photo-Optical Instrumentation Engineers (SPIE) Conference Series, Vol. 5498, Society of Photo-Optical Instrumentation Engineers (SPIE) Conference Series, ed. C. M. Bradford, P. A. R. Ade, J. E. Aguirre, J. J. Bock, M. Dragovan, L. Duband, L. Earle, J. Glenn, H. Matsuhara, B. J. Naylor, H. T. Nguyen, M. Yun, & J. Zmuidzinas, 1–10

Grainge, K., Jones, M., Pooley, G., Saunders, R., & Edge, A. 1993, MNRAS, 265, L57+

Haiman, Z., Mohr, J. J., & Holder, G. P. 2001, ApJ, 553, 545

Herbig, T. 1994, PhD thesis, AA(California Inst. of Tech., Pasadena, CA.)

Holder, G., Haiman, Z., & Mohr, J. J. 2001, ApJ, 560, L111

Holzapfel, W. L., Arnaud, M., Ade, P. A. R., Church, S. E., Fischer, M. L., Mauskopf, P. D., Rephaeli, Y., Wilbanks, T. M., & Lange, A. E. 1997, ApJ, 480, 449

Johnston, D. E., Sheldon, E. S., Tasitsiomi, A., Frieman, J. A., Wechsler, R. H., & McKay, T. A. 2007a, ApJ, 656, 27

Johnston, D. E., Sheldon, E. S., Wechsler, R. H., Rozo, E., Koester, B. P., Frieman, J. A., McKay, T. A., Evrard, A. E., Becker, M. R., & Annis, J. 2007b, ArXiv e-prints

Jones, M., Saunders, R., Alexander, P., Birkinshaw, M., Dilon, N., Grainge, K., Hancock, S., Lasenby, A., Lefebvre, D., & Pooley, G. 1993, Nature, 365, 320

Kaneko, T. 2006, in Society of Photo-Optical Instrumentation Engineers (SPIE) Conference Series, Vol. 6267, Society of Photo-Optical Instrumentation Engineers (SPIE) Conference Series

Komatsu, E., Matsuo, H., Kitayama, T., Hattori, M., Kawabe, R., Kohno, K., Kuno, N., Schindler, S., Suto, Y., & Yoshikawa, K. 2001, PASJ, 53, 57

Majumdar, S. & Mohr, J. J. 2003, ApJ, 585, 603

Mather, J. C., Cheng, E. S., Cottingham, D. A., Eplee, Jr., R. E., Fixsen, D. J., Hewagama, T., Isaacman, R. B., Jensen, K. A., Meyer, S. S., Noerdlinger, P. D., Read, S. M., Rosen, L. P., Shafer, R. A., Wright, E. L., Bennett, C. L., Boggess, N. W., Hauser, M. G., Kelsall, T., Moseley, Jr., S. H., Silverberg, R. F., Smoot, G. F., Weiss, R., & Wilkinson, D. T. 1994, ApJ, 420, 439

Motl, P. M., Hallman, E. J., Burns, J. O., & Norman, M. L. 2005, ApJ, 623, L63

Myers, S. T., Baker, J. E., Readhead, A. C. S., Leitch, E. M., & Herbig, T. 1997, ApJ, 485, 1

Nagai, D. 2006, ApJ, 650, 538

Niemack, M. D., Jimenez, R., Verde, L., Menanteau, F., Panter, B., & Spergel, D. 2009, ApJ, 690, 89

Pavlinsky, M., Hasinger, G., Parmar, A., Fraser, G., Churazov, E., Gilfanov, M., Sunyaev, R., Vikhlinin, A., Predehl, P., Piro, L., Arefiev, V., Tkachenko, A., Pinchuk, V., & Gorobets, D. 2006, in Society of Photo-Optical Instrumentation Engineers (SPIE) Conference Series, Vol. 6266, Society of Photo-Optical Instrumentation Engineers (SPIE) Conference Series

Press, W. H., Teukolsky, S. A., Vetterling, W. T., & Flannery, B. P. 2007, Numerical Recipes, 3rd edn. (Cambridge University Press)

Ruhl, J., Ade, P. A. R., Carlstrom, J. E., Cho, H.-M., Crawford, T., Dobbs, M., Greer, C. H., Halverson, N. w., Holzapfel, W. L., Lanting, T. M., Lee, A. T., Leitch, E. M., Leong, J., Lu, W., Lueker, M., Mehl, J., Meyer, S. S., Mohr, J. J., Padin, S., Plagge, T., Pryke, C., Runyan, M. C., Schwan, D., Sharp, M. K., Spieler, H., Staniszewski, Z., & Stark, A. A. 2004, in Society of Photo-Optical Instrumentation Engineers (SPIE) Conference Series, Vol. 5498, Society of Photo-Optical Instrumentation Engineers (SPIE) Conference Series, ed. C. M. Bradford, P. A. R. Ade, J. E. Aguirre, J. J. Bock, M. Dragovan, L. Duband, L. Earle, J. Glenn, H. Matsuhara, B. J. Naylor, H. T. Nguyen, M. Yun, & J. Zmuidzinas, 11–29

Rykoff, E. S., McKay, T. A., Becker, M. R., Evrard, A., Johnston, D. E., Koester, B. P., Rozo, E., Sheldon, E. S., & Wechsler, R. H. 2008, ApJ, 675, 1106

Sarazin, C. L. 1988, X-ray emission from clusters of galaxies (Cambridge Astrophysics Series, Cambridge: Cambridge University Press, 1988)

Shaw, L. D., Holder, G. P., & Bode, P. 2008, ApJ, 686, 206

Springel, V., White, S. D. M., Jenkins, A., Frenk, C. S., Yoshida, N., Gao, L., Navarro, J., Thacker, R., Croton, D., Helly, J., Peacock, J. A., Cole, S., Thomas, P., Couchman, H., Evrard, A., Colberg, J., & Pearce, F. 2005, Nature, 435, 629

Stanek, R., Rudd, D., & Evrard, A. E. 2009, MNRAS, 394, L11

Sunyaev, R. A. & Zeldovich, I. B. 1980, ARA&A, 18, 537

Sunyaev, R. A. & Zeldovich, Y. B. 1972, Comments on Astrophysics and Space Physics, 4, 173

The Dark Energy Survey Collaboration. 2005, ArXiv Astrophysics e-prints

Voit, G. M. 2005, Reviews of Modern Physics, 77, 207